DNS study on viscoelastic effect in drag-reduced turbulent channel flow

Takahiro Tsukahara[†*], Takahiro Ishigami[†], Bo Yu[‡], Yasuo Kawaguchi[†]

[†]Department of Mechanical Engineering, Tokyo University of Science, Yamazaki 2641, Noda-shi, Chiba 278-8510, Japan; [†]Department of Mechanical Engineering, Beijing University of Petroleum, Changping, Beijing 102200, China

Abstract

The effect of viscoelastic contribution on wall-bounded turbulent flow of drag-reducing surfactant solution is investigated through direct numerical simulations (DNS). A series of DNS on turbulent channel flow is performed for different rheological properties at two different Reynolds numbers. It is found that high drag reduction is achieved by suppressing the turbulent contribution for high Weissenberg number, and/or by decreasing the viscosity ratio and the effective viscosity. A highly drag-reduced turbulent flow at a high Reynolds-number is caused mainly by the viscoelastic effect in the elastic layer whereas the outer-layer flow hardly affects the drag reduction. Moreover, we focus on the viscoelastic contribution term in the budget of Reynolds stress and its relation to the local flow pattern. It is shown that, in the near-wall region of the highly drag-reduced flow, a positive work done by viscoelastic stress is closely associated with vortex stretching that produces turbulent kinetic energy from stored elastic energy, whereas a negative one causes vortex compression.

Keywords: Non-Newtonian fluid; Direct Numerical simulation; Drag reduction; Turbulent channel flow; Topological classification

*Corresponding author

Email address: tsuka@rs.noda.tus.ac.jp (Takahiro Tsukahara[†])

Please cite this article as: Tsukahara, T., et al. DNS study on viscoelastic effect in drag-reduced turbulent channel flow. J. Turbulence, Vol. 12 (2011), No. 13, 1–25. doi:10.1080/14685248.2010.544657

1. Introduction

As has been well known for sixty years, turbulent friction drag can be reduced by up to 80% through the addition of minute amounts of polymers or surfactants to water. The observation by Toms [1] triggered a number of studies that attempted to characterize the phenomenon and apply it to practical engineering problems. Indeed, surfactant-induced DR is a useful technique for reducing the pumping power used in district heating and cooling systems. One promising additive is a cationic surfactant of cetyltrimethyl ammonium chloride (CTAC) under appropriate conditions of surfactant chemical structure, concentration, temperature, and so on, to create a micellar network in the surfactant solution. The resulting microstructure gives rise to viscoelasticity in the solution. Consequently it is important to investigate the characteristics of turbulence of viscoelastic fluids.

There have been many studies on DR by either polymer or surfactant additives, and several comprehensive reviews [2, 3, 4, 5] provide some highlights of the progress in understanding of this subject. A number of experimental studies have been increasingly carried out, in part because the subject lies at the intersection of two complex and important fields of rheology and turbulence. Although it is practically difficult to analyze the interaction between additives and turbulent motions at the molecular level, many key aspects of drag-reduced turbulent flow by adding polymers have gradually been elucidated. For instance, we have already known that additives inhibited the transfer of energy from the streamwise to the wall-normal velocity fluctuations, and that the strong vorticity fluctuation near the wall disappeared in the drag-reducing flow. Recent experiments on CTAC-solution channel flows reported that the drag-reducing CTAC additives reduced the frequency of turbulent bursting events near the wall, and its characteristics were not only dependent on drag-reduction level but also on concentration of additives. Therefore, a parametric study should be expected to ascertain the influences of the surfactant property and the concentration of additives [6, 7, 8].

Direct numerical simulation (DNS) has become an important tool to study the physics of turbulence and make it possible to identify instantaneous flow structures in turbulence. Although employing constitutive equations derived from modeling the polymer molecules, DNS has been used to study the drag-reduced turbulent flow by polymer additives [9, 10, 11, 12, 13, 14, 15, 16, 17, 18, 19], and confirmed that viscoelastic models can reproduce most of the experimental observations (such as wider buffer layer, reduction of Reynolds

shear stress and larger spacing between low-speed streaks). Although there are competing models (e.g., FENE-P, Oldroyd-B), we selected the Giesekus model [20] for our study because this model can describe well the measured apparent shear viscosity and extensional viscosity of the surfactant solution: cf. Wei *et al.* [21]. On the other hand, the FENE-P model was shown to be able to reproduce the essential effect of polymers and provided evidences that polymers disrupt the near-wall turbulence regeneration cycle and reduce the turbulent friction drag (see, for example, White & Mungal [5]). As for surfactant additives, Suzuki *et al.* [22] studied numerically drag-reduced flow using the Giesekus model. The author's group [23, 24, 25, 26] has simulated viscoelastic fluids by DNS with the Giesekus model. These works have provided ample, albeit qualitative, evidences that many of the phenomena that have been experimentally observed in association with drag reduction in the presence of surfactant additives can also be predicted by DNS using the Giesekus model, indicating that this model is appropriate for surfactant solutions. One of the objectives of the present work is to carry out a similar, but much more quantitative and systematic, numerical investigation.

In this study, we consider dilute surfactant solutions, in which the shear-thinning behavior is assumed to be negligible, but the elongational viscoelastic effect is taken into account using a method for the extra elastic stresses. Then we perform a series of DNS, using the Giesekus model, of surfactant-based drag-reducing turbulent flow in a wide range of drag-reduction rate at different Reynolds numbers. Through this, we investigate aspects of the coupling between fluid rheology and amount of DR. In the contexts of the budget of the energy transport equation and the flow topology, we examine how the energy is transferred between turbulent kinetic energy and elastic energy. From this, we attempt to identify the role and influence of viscoelasticity in drag-reducing effect on the structures of turbulent channel flow.

2. Numerical procedure

A series of DNS on a channel flow of viscoelastic fluid is performed at two different friction Reynolds numbers of $Re_{\tau 0} = u_\tau \delta / \eta_0 = 150$ and 395 based on the friction velocity u_τ, the channel half width δ, and the kinematic viscosity η_0 of the viscoelastic solution. We consider a turbulent flow which is driven by the mean pressure gradient and is assumed to be fully developed, denoting the streamwise direction as x, the wall-normal direction as y, and the spanwise direction as z. The configuration of the plane channel is shown

in Fig. 1, and the computational conditions are given in Table 1. The periodic boundary condition is employed in the horizontal direction, and the non-slip boundary condition is imposed on the walls. In this paper, u, v, and w are velocity components in the x, y, and z directions, respectively.

We employ a viscoelastic Giesekus constitutive equation to calculate the extra stress caused by the interaction between shear rate and the elasticity network structure of surfactant additives. The dimensionless governing equations for an incompressible viscoelastic-fluid flow can be written as follows: the continuity equation

$$\frac{\partial u_i^+}{\partial x_i^*} = 0, \tag{1}$$

the Navier-Stokes equation

$$\frac{\partial u_i^+}{\partial t^*} + u_j^+ \frac{\partial u_i^+}{\partial x_j^*} = -\frac{\partial p^+}{\partial x_i^*} + \frac{\beta}{Re_{\tau 0}} \frac{\partial}{\partial x_j^*} \left(\frac{\partial u_i^+}{\partial x_j^*} \right) + \frac{(1-\beta)}{We_\tau} \frac{\partial c_{ij}^+}{\partial x_j^*} + \frac{\partial \overline{p}^+}{\partial x_1^*} \delta_{1i}, \tag{2}$$

and the constitutive equation for the conformation tensor c_{ij} associated with deformation of network structures, based on the Giesekus model [20]

$$\begin{aligned} &\frac{\partial c_{ij}^+}{\partial t^*} + \frac{\partial u_k^+ c_{ij}^+}{\partial x_k^*} - \frac{\partial u_i^+}{\partial x_k^*} c_{kj}^+ - \frac{\partial u_j^+}{\partial x_k^*} c_{ki}^+ \\ &= -\frac{Re_{\tau 0}}{We_\tau} \left[c_{ij}^+ - \delta_{ij} + \alpha \left(c_{ik}^+ - \delta_{ik} \right) \left(c_{kj}^+ - \delta_{kj} \right) \right], \end{aligned} \tag{3}$$

where u_i and p denote the velocity vector and the pressure, respectively, and δ_{ij} the Kronecker delta. The quantities with superscript + indicate that they are normalized by u_τ and η_0, while those with $*$ denote normalization by u_τ and δ. In Eq. (3) the mobility factor, which is a parameter determining the extensional viscosity, is set to be $\alpha = 0.001$. As for a rheological property of fluids, the parameter β $(= \eta_s/\eta_0)$ is the ratio of solvent contribution η_s to the total zero-shear viscosity η_0, and ranges from 0 to 1. Equation (2) can be reduced to that for a Newtonian fluid, if β is set to 1. The Weissenberg number

$$We_\tau = \frac{\text{relaxation time}}{\text{viscous timescale}} = \frac{\lambda}{\eta_0/u_\tau^2} \tag{4}$$

is chosen to be 10–40.

Time advancement is done by the second-order Adams-Bashforth method, but the second-order Crank-Nicolson method is used for the viscous terms

in the wall-normal direction. For the spatial discretization, the finite difference method is adopted. The numerical scheme with fourth-order accuracy is employed in the streamwise and spanwise directions, and second-order accuracy is applied in the wall-normal direction. It is well known that high Weissenberg-number problem, namely breakdown of the calculation at a high We_τ, has to be solved to reach a converged solution for viscoelastic flows. Thus in order to prevent numerical instability, special attention should be paid to the numerical modeling of the convective term in the constitutive equations. In the present simulation, the second-order MINMOD scheme is implemented for the convective term in the constitutive equation without any additional term, although the numerical diffusivity term was introduced (artificial diffusion scheme) in earlier studies by other researchers. The MINMOD scheme (almost identical to SOUCUP scheme) is a composite scheme consisting of the second-order upwind, central differencing and first-order upwind schemes, the switch between them being controlled by a convection boundedness criterion [27]. Therefore, this MINMOD flux-limiter scheme essentially involves numerical diffusion, and successfully stabilizes the present simulations without adding artificial diffusivity term. It should also be noted that this scheme is relatively more diffusive than other composite schemes, but shows low-dispersion characteristics of the high-order schemes (compared to a single use of first-order scheme) [27, 28]. In addition, our previous work [23] reported that the MINMOD scheme stabilized the simulation of viscoelastic flow at high Weissenberg number, whereas the artificial diffusion scheme required large artificial diffusivity to stabilize the calculation.

3. Results and discussion

We investigated effects of the various rheological parameters on the drag reduction by systematically varying β and We_τ. In presenting the DNS results which follow, we attempt to study the correlation between some turbulence statistics and achieved drag-reduction rates. Table 2 summarizes the test parameters and some important mean-flow variables for a Newtonian fluid and several types of viscoelastic fluids. The effective wall kinematic viscosity η_{eff} given in the table is calculated from the proportionality between the total wall shear stress $\tau_w = \rho u_\tau^2$ and the mean velocity gradient at the wall as follows:

$$\left|\frac{\tau_w}{\rho}\right| = \eta_{eff}\left|\frac{\mathrm{d}\overline{u}}{\mathrm{d}y}\right|_{y=0}. \tag{5}$$

Based on η_{eff}, we introduce two kinds of actual Reynolds numbers of $Re_\tau = u_\tau \delta/\eta_{eff}$ and $Re_\mathrm{m} = 2U_\mathrm{m}\delta/\eta_{eff}$, where U_m is the bulk mean velocity, and corresponding values for each fluid are also given in Table 2. Note that u_τ is defined for each drag-reduced flow state (but not the corresponding Newtonian case), since the externally imposed pressure gradient along the x direction is fixed at each $Re_{\tau 0}$. In the following subsection, we define the drag-reduction rate $DR\%$ and discuss its dependence on Re_m and the rheological parameters.

3.1. Drag-reduction rate

The friction coefficient is defined as the non-dimensional wall shear stress of τ_w:

$$C_f = \frac{\tau_w}{\frac{1}{2}\rho U_\mathrm{m}^2} = \frac{2}{U_\mathrm{m}^{+2}}, \tag{6}$$

where ρ is the density of fluid. Figure 2(a) presents the results obtained here against the bulk Reynolds number for different values of the rheological parameters. The friction coefficient in the turbulent regime for a Newtonian fluid is represented by Dean's empirical correlations [29]:

$$C_f = 0.073 Re_\mathrm{m}^{-0.25}. \tag{7}$$

The limiting equation proposed by Virk [30, 31], who examined friction factor and velocity profile results for a large number of high polymer solutions, which is called Virk's maximum-drag-reduction asymptote (MDR), is

$$\frac{1}{\sqrt{C_f}} = 19.0 \log\left(Re_\mathrm{m}\sqrt{C_f}\right) - 32.4. \tag{8}$$

Although originally proposed for a pipe flow, this relation has been believed to be applicable to a channel flow [32, 33, 34].

As can be seen clearly in Fig. 2(a), DR occurs for viscoelastic fluids (cases except for fluids A1 and A2). When we increase We_τ at the fixed $Re_{\tau 0}$ of 150, the value of C_f approaches the MDR. In our simulations, as the mean pressure drop is kept constant, the DR is accompanied by an increase of the bulk mean velocity, i.e., Re_m. The highest value of the Weissenberg number ($We_\tau = 40$, fluid G) gives rise to C_f of almost the MDR. Note that it is not surprising that asymptotic surfactant solutions can lead to greater DR than that predicted by the MDR for polymer surfactants. Indeed, a number of

researchers using surfactant drag-reducing additives have reported somewhat higher levels of DR than Virk's suggested correlation (cf., Zakin *et al.* [35] and references therein).

Figure 2(b) shows the same data as that of Fig. 2(a), but plotted as the drag-reduction rate $DR\%$ versus Re_{m}. Usually the amount of drag reduction is expressed as the reduction of C_f due to the additives compared to a corresponding Newtonian flow at the same level of Re_{m}. In addition, Housiadas & Beris [16] proposed the following relationship between $DR\%$ and U_{m}:

$$DR\% = \frac{C_{f\,\mathrm{Newt}} - C_{f\,\mathrm{visc}}}{C_{f\,\mathrm{Newt}}} = 1 - \left(\eta^{+}_{eff}\right)^{2(1-n)/n} \left(\frac{U^{+}_{\mathrm{m\,Newt}}}{U^{+}_{\mathrm{m\,visc}}}\right)^{2/n}_{Re_{\tau 0}}, \qquad (9)$$

where the suffixes 'visc' and 'Newt' stand for values in a viscoelastic flow and Newtonian flow, respectively, and $n = 1.1713$. Utilizing this relationship, we have computed $DR\%$ since DNS Newtonian data at each $Re_{\tau 0}$ are available . The result indicates that the viscoelastic flows with higher $DR\%$ are mainly related to an increase of We_τ (see also Table 2). For instance, a slight increase of $We_\tau = 10 \rightarrow 11$ (fluids C to D1) induces a rise of 5% in $DR\%$. This increment is relatively large compared with that from fluids E1 to G ($We_\tau = 30 \rightarrow 40$). This is because the C_f and $DR\%$ of fluids E1 and G are close to Virk's MDR asymptote whereas those of fluids C and D1 are approximately turbulence values, as given in Fig. 2(a). In a high-$DR\%$ flow at high We_τ (fluids E1, E2, F, and G), the production and redistribution of streamwise velocity fluctuations are suppressed, as discussed later.

A comparison between fluids E1 and F (or fluids B and C) also indicates that the $DR\%$ increases with the decrease of β at a constant $Re_{\tau 0}$. In this case, η_{eff} decreases, accompanied by a decrease in C_f and an increase in $DR\%$. If we focus on the Reynolds-number dependence, a comparison between fluid E1 and E2 (as well as D1 and D2) indicates that no meaningful distinction in $DR\%$ and in η_{eff}/η_0 is found between two different Reynolds numbers, as implied in Table 2.

Based on the above discussion, we would propose two aspects of the coupling between fluid rheology and amount of $DR\%$. The first aspect is a decrease of turbulence contribution by increasing We_τ, and the second one is a decrease of the effective viscosity by decreasing β. Through these aspects, DR is enhanced. In the following sections we present various turbulence statistics to discuss these two aspects.

3.2. Mean velocity profiles

The mean velocity profiles are plotted in semi-logarithmic coordinates in Fig. 3, including the experimental data obtained by Yu *et al.* [24]. In their experiment, a $DR\%$ of 51% was achieved using a surfactant solution of cetyltrimethyl ammonium chloride dissolved in water with a concentration of 75 ppm. Here, the abscissa is the renormalized distance from the wall, $y_\eta = yu_\tau/\eta_{eff}$, based on the viscous length of the effective viscosity η_{eff}. Note that, for Newtonian turbulent flow, $y_\eta = y^+$.

The present results in Fig. 3 are in qualitative agreement with their data. All profiles collapse to the linear law of the wall in the viscous sublayer. Further away from the wall, however, the velocity of the viscoelastic flow increases compared to the Newtonian case (fluids A1 and A2). The dotted line in Fig. 3 is Virk's asymptote for MDR [31]:

$$\overline{u}^+ = 11.7 \ln y_\eta - 17.0. \tag{10}$$

The zone in which the velocity profile follows this asymptote is called the elastic layer, since the solution exhibits an elastic flow behaviour in this layer [4]. For $y_\eta > 10$ the profiles of fluids E1–G with high $DR\%$ of more than 50% are close to Eq. (10), while those of the other fluids are not. In the logarithmic region, where the flow is represented by $\overline{u}^+ = 2.5 \ln y_\eta + B$, there exists a noticeable discrepancy between the Newtonian flow (fluid A1) and the viscoelastic flows (fluids B–G). The logarithmic profiles for viscoelastic flows are shifted upwards parallel to that of Newtonian flow. The upward shift of the log-law profile is known to be equivalent to DR [2, 4]. In Fig. 3 we observe that the magnitude of the shift seems to depend mainly on We_τ. The log-law profiles for $We_\tau = 30$ (fluids E1, E2, and F) can be observed from a position higher than that of Newtonian flow. However, the case of fluid G with $We_\tau = 40$, in which the highest $DR\%$ in the present study is achieved, reveals no apparent log-law region between the elastic layer and the outer layer. The same behavior is seen in the experimental results of Yu *et al.* [24] and others [33, 34] (not shown here). The existence of log-law region in fluid F implies a wide scale range of turbulent vortices in the flow. Therefore, the turbulent contribution to the momentum transfer is not so different between fluids E1 and F. It can be conjectured that the high $DR\%$, which has been obtained in fluid F, is attributed to a decrease of the effective viscosity rather than suppressing turbulent motions, thus inducing a thinning of the viscous sublayer by a relative decrease of β. As β decreases with a fixed We_τ, η_{eff}/η_0

decreases accompanied by an increase of $DR\%$ (see fluids B $\rightarrow$ C and E1 $\rightarrow$ F in Table 2).

Note that the given friction Reynolds numbers for both fluids D2 and E2 are different from the other cases, but the rheological parameters are the same as those of fluids D1 and E1, respectively. Comparison between them reveals that the shift displacement of the log-law from the Newtonian profile is almost the same magnitude regardless of the Reynolds number, as shown in Fig. 3. In addition, there was less discrepancy in $DR\%$ between two different Reynolds-number flows, i.e., fluids D1 and D2 (also E1 and E2): see Fig. 2(b). An increase of $Re_{\tau 0}$ with constant We_τ denotes an enlargement of the channel width, because the parameters of u_τ, η_0, and λ are constant for the same fluid: if $Re_{\tau 0}$ increases due to an increase in the driving force, the value of We_τ also increases in proportion to the square of u_τ. In other words, for a given $Re_{\tau 0}$ and We_τ, the channel width (2δ) still appears as another parameter. Therefore the lower dependence on the Reynolds number when the parameters of rheological properties are fixed implies that $DR\%$ is a strong function of u_τ and λ in Eq. (4). This dependency is similar to the 'diameter effect' observed in pipe flow experiments [36, 37].

3.3. FIK identity

According to Fukagata *et al.* [38], the friction coefficient can be decomposed into a viscous contribution (referred as a laminar contribution in [38]), a turbulent contribution, and inhomogeneous and transient contributions. They proposed a direct relation between the skin friction coefficient and the Reynolds stress distribution and established an identity equation for three canonical wall-bounded flows (including channel flow). Based on a similar procedure, the equation for a fully-developed channel flow of a viscoelastic fluid, which is governed by Eq. (2), is derived as,

$$\begin{aligned} C_f = 12\frac{\beta}{Re_\mathrm{m}} &+ \frac{6}{U_\mathrm{m}^{+2}}\int_0^1 \left(-\overline{u'^+v'^+}\right)(1-y^*)\,\mathrm{d}y^* \\ &+ \frac{6}{U_\mathrm{m}^{+2}}\int_0^1 \frac{c_{xy}^+(1-\beta)}{We_\tau}(1-y^*)\,\mathrm{d}y^*. \end{aligned} \tag{11}$$

The first term is the viscous contribution, which is identical to the well-known laminar solution. The second and third terms are, respectively, the turbulent contribution proportional to the weighted Reynolds stress and the viscoelastic contribution proportional to the weighted viscoelastic stress. These terms

further suggest that near-wall turbulent motions, which induce strong shear stresses, are more responsible for the frictional drag than the turbulence in the outer layer, where the Reynolds shear stress and the viscoelastic stress are dominant in the total shear.

The above perspective, often referred to as the FIK identity, is useful for analyzing the elements of the DR [24, 39]. Figure 4 shows the fractional contributions made by each term for five typical cases. The reduction of the frictional coefficient C_f for viscoelastic fluid is attributed mainly to the reduction of the turbulence contribution, although there is an additional viscoelastic contribution with a small, but not trivial, value of about 0.001. In all cases of the present simulations, the effect of reduction of the turbulence contribution on C_f exceeds that of onset of the viscoelastic contribution, resulting in a positive $DR\%$. The turbulence contribution for fluid G ($We_\tau = 40$) is very small and becomes comparable to the other contribution components, whereas that for fluid C ($We_\tau = 10$) remains dominant. It is conjectured that this contribution decreases with the increase of the Weissenberg number.

Figure 5 presents the weighted Reynolds shear stress as appearing in Eq. (11). As also mentioned in the previous section, a high value of the Weissenberg number affects DR by damping the turbulent vortical motion and decreasing the Reynolds shear stress. Its behavior for fluid F is almost the same or slightly higher than that for fluid E1, where the same value of We_τ is given. Hence the turbulence contributions for these cases are at the same level. It should also be noted that the C_f of fluid F is lower than that of fluid E1. This is caused by the reduction of the viscous contribution, which is attributed to a decrease of the effective viscosity η_{eff} for low β. This is why the obtained $DR\%$ for fluid F is comparable to that of a higher-We_τ fluid (G). Again, it is worth noting that, although fluids F and G yield almost the same high $DR\%$, the former gives a smaller viscous contribution and a larger turbulence contribution than those of the latter case. In brief, a low β (such as for fluid F) induces a decrease of the viscous contribution, and a high We_τ (such as for fluid G) damps down the turbulence contribution.

3.4. Turbulence intensity, Reynolds stress and cross-correlation coefficient

Figures 6–8 show profiles of the turbulence intensities as a function of y_η. It can be seen that, for high-$DR\%$ cases, the value of u'^+_{rms} tends to increase for $y_\eta > 5$ and both v'^+_{rms} and w'^+_{rms} decrease in the whole channel width (see (a) in the figures). In other words, the flow at high $DR\%$ is prone to become anisotropic turbulence. The peak positions of v'^+_{rms} and w'^+_{rms} for viscoelastic

flow shift away from the wall as $DR\%$ increases. This is consistent with the shift of the logarithmic region in the $\overline{u}^+$ profile shown in Fig. 3.

As seen from Fig. 6(b), the profiles of $u'^+_{\rm rms}$ for rheologically identical fluids (e.g., fluids D1 and D2 at constant We_τ and β) are independent of the Reynolds number, $Re_{\tau 0}$. On the other hand, discrepancies due to the Reynolds-number dependence are found in the other two components of $v'^+_{\rm rms}$ and $w'^+_{\rm rms}$, as shown in Figs. 7(b) and 8(b) respectively. This seems to be an effect of the low Reynolds number. Antonia *et al.* [40] and Abe *et al.* [41] indicated that the Reynolds-number dependencies for $v'^+_{\rm rms}$ and $w'^+_{\rm rms}$ are significant compared to that for $u'^+_{\rm rms}$: the wall-normal and spanwise components are enhanced with increasing $Re_{\tau 0}$, because the energy redistribution increases for them. However, the $v'^+_{\rm rms}$ of fluids E1 and E2 for $y_\eta < 40$ (and also those of D1 and D2 for $y_\eta < 20$) do not differ much from each other. In this respect we note that the wall-normal velocity fluctuation in the elastic layer of viscoelastic flow is suppressed to a certain degree that depends on the level of $DR\%$.

In a case where the near-wall value of $v'^+_{\rm rms}$ is reduced, the Reynolds shear stress also becomes very small in the near-wall region. Figure 9 shows the $-\overline{u'^+v'^+}$ distribution. We see that the peak value of the $-\overline{u'^+v'^+}$ decreases monotonically with increasing We_τ. Also, the location of the peak moves continuously away from the wall with increasing We_τ. This behavior gives rise to a significant decrease of C_f (i.e., an increase of $DR\%$), as suggested by Eq. (11).

As described above and by other researchers [9, 24, 34, 6], it has been elucidated that under DR conditions the Reynolds shear stress of $-\overline{u'^+v'^+}$ is strongly damped. The reduction of $-\overline{u'^+v'^+}$ should be responsible for a decrease in the magnitude of the correlation between the streamwise velocity fluctuation u' and the wall-normal component v' as well as in the magnitude of v'. The profile of the cross-correlation coefficient

$$R_{uv} = \frac{-\overline{u'^+v'^+}}{u'^+_{\rm rms} v'^+_{\rm rms}} \tag{12}$$

is shown in Fig. 10. It is already known that R_{uv} for Newtonian turbulent channel flow is less dependent on the Reynolds number, and that the value except for the wall vicinity and channel center lies around 0.4 [43, 42]. It is clearly seen that R_{uv} for turbulent viscoelastic flow becomes small compared to the Newtonian cases. In particular, the reduction of R_{uv} is noticeable in the near-wall region, and its diminution seems to depend on the magnitude

of $DR\%$. Compared to the other fluids, R_{uv} of fluid G is much smaller throughout the channel—note that a point where $R_{uv} = 0$ indicates the channel center. In addition, a secondary peak of R_{uv} near the channel center can be observed in the Newtonian (fluid A1) and low-$DR\%$ cases (B–D), but R_{uv} for high-$DR\%$ cases at $Re_{\tau 0} = 150$ (fluids E1, F, and G) monotonically decreases as it approaches the channel center. This suggests that turbulent structures in highly drag-reduced flow are damped also in the outer layer.

3.5. Anisotropy characteristic

It is interesting to analyze the relation between DR and the anisotropy of the Reynolds stresses to clarify the dynamics of drag-reduced turbulence. Turbulence anisotropy can be quantified by examining the anisotropy invariant map (AIM) proposed by Lumley & Newman [44], as shown in Fig. 11(a). The anisotropy tensor

$$b_{ij} = \frac{\overline{u_i' u_j'}}{2k} - \frac{1}{3}\delta_{ij} \quad \left(k = \frac{1}{2}\overline{u_i' u_i'}\right), \tag{13}$$

satisfies its characteristic polynomial, where its second and third invariants of b_{ij} are given by

$$\mathrm{II} = b_{ij} b_{ji} \tag{14}$$

$$\mathrm{III} = b_{ij} b_{jk} b_{ki} \tag{15}$$

While II measures the intensity of the anisotropy, the shape of eddies is characterized by III [45]. Due to realizability conditions for the Reynolds stress tensor, the possible values of II and III must be within the triangle area in Fig. 11(a). This region is bounded by three lines, namely the two-component turbulence state, $2 - 9\mathrm{II} + 18\mathrm{III} = 0$, and two axisymmetric states, $6\mathrm{II}^3 - \mathrm{III}^2 = 0$. For the axisymmetric states, positive III represents the rod-like turbulence strained by axisymmetric expansion, and negative III describes the disk-like turbulence by axisymmetric contraction. The intersections of the bounding lines can be found at $(\mathrm{III}, \mathrm{II}) = (0, 0)$, $(\frac{2}{9}, \frac{2}{3})$, and $(-\frac{1}{36}, \frac{1}{6})$, each corresponding to the isotropic, one-component, and two-component axisymmetric states of turbulence, respectively.

Figure 11(b) shows the AIM for the Newtonian and viscoelastic flows. A typical trend in trajectories of the data can be clearly distinguished regardless of the fluid properties. In the wall vicinity, v'_{rms} is negligible compared

to the other components, so the invariants reside near the upper boundary which represents the two-component state. As y increases from zero through the sublayer, the data point approaches the one-component limit state with the streamwise turbulence intensity larger than the other direction components. After that, data curves along the axisymmetric boundary (rod-like turbulence) towards the isotropic state as y comes close to the channel center. It can clearly be seen that the anisotropy of near-wall turbulence ($y \to 0$) is shifted to higher values as $DR\%$ increases. Especially, highly drag-reduced flows (fluids E1, F, and G) reveal a noticeable trend that turbulence in the central region of the channel tends toward the axisymmetric (or one-component) turbulence state rather than isotropic turbulence, ($v'^{+}_{\mathrm{rms}} < w'^{+}_{\mathrm{rms}} \ll u'^{+}_{\mathrm{rms}}$). Since in such a state there is less Reynolds shear stress of $-\overline{u'^{+}v'^{+}}$, the sole production for $\overline{u'^{+}u'^{+}}$ in turbulent channel flow,

$$P = -2\overline{u'^{+}v'^{+}}\frac{\partial \overline{u}^{+}}{\partial y^{+}}, \tag{16}$$

decreases consequently. These trend of increased anisotropy in the entire channel is observed if the Reynolds number in Newtonian turbulent flows is reduced. This results obtained for DNS of surfactant DR are in close agreement with those obtained by DNS studies [46, 47], which reported that the polymer-induced DR should be accompanied by increasing anisotropy in the near-wall region. They demonstrated that turbulence with drag-reducing polymer additives forces the polymer chains to stretch in the mean-flow direction and, through this process, turbulent fine-scale eddies are restructured into axisymmetric flows: see Jovanović *et al.* [46] for a full discussion of this topic.

To clarify the difference between the fluids considered here, we plot the profiles of the second invariant II, which represents the degree of anisotropy, as a function of the dimensionless wall distance of the inner or outer scaling in Fig. 12. In Fig. 12(a), the value of II increases with increasing $DR\%$, showing a significant difference between the high $DR\%$ cases (fluids E–G) and the others. Moreover, the peak location seems to shift away from the wall and widen in the elastic layer, the one-component state area being extended. The distributions for fluids F and G, where $DR\% > 60$ is achieved, show good collapse throughout the channel if plotted against y_η. This may imply that the maximum level of DR has been obtained by the fluids, at least for the present Reynolds number.

In contrast to the inner scaling, we can find a collapse in the outer layer (generally, $y/\delta > 0.2$ in Newtonian flow) if we focus on the plot with the outer scaling, given in Fig. 12(b). The profiles of rather low $DR\%$ fluids (C and D1) are matched very well. It is interesting to note that the behavior for fluid E2 is close to them, whereas fluid E2 gives a rather high $DR\%$ of 52.5%. Although this collapse might be a coincidence, we conjecture that, in the outer layer, a moderately drag-reduced turbulence is qualitatively similar to a low-$DR\%$ (or no DR) turbulence at a lower Reynolds number. As for the inner layer, the profile for fluid E2 is approximately the same as those of the highest $DR\%$ cases (fluids F and G): see Fig. 12(a). Thus it can be concluded that a high DR in a high Reynolds-number turbulent flow is caused mainly by the viscoelastic effect in the elastic layer whereas the outer-layer flow remains almost Newtonian flow. Recently, a similar concept was reported for experiments of surfactant solutions by Watanabe *et al.* [48]. They demonstrated that a shear-induced structure (SIS) exists in the near-wall region, but not in the outer layer due to the mixing potential of turbulence. Here, SIS is a state where moderate shear stress assists the formation of a micellar network and this network expresses the viscoelasticity of fluid, cf. [49]. This bilayered structure model with viscoelastic (SIS) and non-viscoelastic fluids (non-SIS) has been observed also in the turbulent boundary layer of drag-reducing surfactant solutions [50, 51].

3.6. Budget of Reynolds stress

In this section we consider the budget terms of the Reynolds normal stress (here, the streamwise component), and then differences which occur between two high-$DR\%$ cases and between high-$DR\%$ and low-$DR\%$ cases are discussed. The balance equation for $\overline{u'^+u'^+}$ in fully-developed channel flow can be expressed as

$$\frac{\mathrm{D}}{\mathrm{D}t}\overline{u'^+u'^+} = P - \varepsilon + \Pi + T + D + E, \tag{17}$$

where the production term P is defined as Eq. (16) and the other terms are

$$\text{dissipation} \quad : \quad \varepsilon = 2\beta\overline{\frac{\partial u'^+}{\partial x_k^+}\frac{\partial u'^+}{\partial x_k^+}}, \tag{18}$$

$$\text{VPG} \quad : \quad \Pi = -2\overline{\left(u'^+\frac{\partial p'^+}{\partial x^+}\right)}, \tag{19}$$

$$\text{turbulent transport} \quad : \quad T = -\frac{\partial}{\partial x_k^+}\overline{u'^+ u'^+ u_k'^+}, \tag{20}$$

$$\text{molecular diffusion} \quad : \quad D = \beta\frac{\partial^2}{\partial {x_k^+}^2}\overline{u'^+ u'^+}, \tag{21}$$

$$\text{VEC} \quad : \quad E = 2\frac{1-\beta}{\mathrm{We}_\tau}\left(\overline{u'^+\frac{\partial c_{xk}'^+}{\partial x_k^+}}\right). \tag{22}$$

Here, VPG and VEC denote the velocity pressure-gradient correlation term and the viscoelastic contribution term, respectively. The VPG term can be split into pressure strain and pressure diffusion terms: the former term is known to play a dominant role in the energy redistribution, while the latter term is zero for $\overline{u'^+u'^+}$. In Eq. (17), the conformation tensor c_{ij} appears only in the VEC term of Eq. (22), which is an extra term derived from the viscoelastic effect, and it appears as the correlation between velocity and viscoelastic stress fluctuations. Figure 13 shows the budget terms normalized by η_{eff}/u_τ^4 with respect to the viscous wall region for some typical high-$DR\%$ cases. As given in the figure, very good balances are achieved, demonstrating high accuracy in the present DNS. The maximum value of residual is less than 10^{-2} in all cases.

A clear difference between Newtonian (fluid A1) and viscoelastic fluids can be found in the VPG term corresponding to the redistribution term (see Fig. 13). Over most of the channel, negative Π is the dominant sink for $\overline{u'u'}$, while positive Π in the $\overline{v'v'}$ and $\overline{w'w'}$ balances are the dominant energy sources. Thus the reduction of the VEC term represents the inhibition of the transfer of energy to the two other components, inducing the one-component turbulent state. For highly drag-reducing fluids, the VPG term is much smaller than that of Newtonian fluid, and hence the relevant flow strengthens the tendency toward anisotropic turbulence, as discussed for Fig. 11.

Although almost the same $DR\%$ values are obtained in fluids F and G, their budgets compared in Fig. 13 are slightly but significantly different. For instance, the maximum turbulence production in fluid G is apparently smaller than that in fluid F due to higher We_τ. In addition the turbulent transport in fluid G is also moderated so the relevant profile of $\overline{u}$ given in Fig. 3 becomes laminar-like. On the other hand, the magnitudes of the dissipation and the molecular diffusion in fluid G are larger than those in fluid F, which might be due to the small β (i.e., small η_{eff}) of fluid F. These results indicate that high $DR\%$ in fluid G is attributed to the suppression of turbulence

production and that in fluid F is due to the decrease of effective viscosity. It is also noteworthy that the difference between the productions in fluids F and G, i.e., the surplus production $\Delta P = P_{\mathrm{F}} - P_{\mathrm{G}}$, almost balances with that of VEC, $\Delta E (= E_{\mathrm{F}} - E_{\mathrm{G}})$, as well as turbulent transport, $\Delta T (= T_{\mathrm{F}} - T_{\mathrm{G}})$:

$$\Delta P + \Delta E + \Delta T \approx 0. \tag{23}$$

This means that the VEC term for fluid F is more effective as a dissipation and diffusion term. In the next section, we will consider this term in more detail.

In Fig. 14 the results of the budget for high and low $DR\%$ cases show a similar behavior to that for the two highest $DR\%$ cases given in Fig. 13, although shown in semi-logarithmic coordinates of y_η. Again we observe smaller magnitudes of production and turbulent transport with increasing We_τ (and $DR\%$), corresponding to smaller turbulence contribution. The much smaller VPG in Fig. 14(a) than in (b) is consistent with the smaller turbulence intensities of the wall-normal and spanwise components (see Figs. 7 and 8). It is of interest that, for the high-$DR\%$ case, the budget terms are less dependent on the Reynolds number throughout the channel, as shown in Fig. 14(a). As can be seen in (b), on the other hand, for the low-$DR\%$ flow as well as Newtonian flow (not shown in the figure), the near-wall values of production, dissipation, molecular diffusion and turbulent transport tend to increase as $Re_{\tau 0}$ increases. Moreover, focusing on the behavior of VEC in the near-wall region, a small bump at $y_\eta \approx 8$ can be found only in the high $DR\%$ cases. It can be construed that the VEC term of the high-$DR\%$ flows (fluids E1, E2, F, and G) works as a gain of turbulent energy in some areas, whereas it works as a dissipation in almost the entire channel. As also for polymer DR, Massah & Hanratty [52] and Min *et al.* [14] showed that the polymer chains absorbed elastic energy in the vicinity of the wall and released it in the buffer and log layers when the relaxation time of the polymers was long enough (meaning the high Weissenberg number). The present results support their proposed DR mechanism.

3.7. Viscoelastic contribution

3.7.1. Decomposition of VEC term

In order to discuss the viscoelastic contribution in more detail, the VEC term of Eq. (22) is divided into E_d and E_ε:

$$E = E_d - E_\varepsilon, \tag{24}$$

transport by viscoelastic stress:

$$E_d = 2\frac{(1-\beta)}{\mathrm{We}_\tau}\frac{\partial}{\partial x_k^+}\overline{u'^+ c'^+_{xk}}, \tag{25}$$

work by viscoelastic stress:

$$E_\varepsilon = 2\frac{(1-\beta)}{\mathrm{We}_\tau}\left(\overline{c'^+_{xk}\frac{\partial u'^+}{\partial x_k^+}}\right). \tag{26}$$

Regarding these two terms, results in several cases are shown in Fig. 15. It can be seen in Fig. 15(a) that energy is convected by E_d from the buffer layer (in $y_\eta = 5$–30) and the elastic layer (i.e., up to $y_\eta = 60$ in the case of fluid G), where the production is high (see Figs. 13 and 14), to the vicinity of the wall $y_\eta < 2$ and the outer layer. On the other hand, E_ε transfers the turbulent energy to the elastic energy in almost the whole channel; hence this term can be interpreted as an 'energy-transfer rate between between the turbulent kinetic energy and the elastic energy'. Negative (positive) $-E_\varepsilon$ means that the kinetic energy carried by velocity fluctuations u'^+ is damped (enhanced) by storage (release) of elastic energy in the micellar structure of the surfactant additive. In the wall vicinity ($y_\eta < 2$), as E_d carries sufficient energy inward to balance $-E$, the VEC term E of Eq. (22) becomes zero there. It is worth noting that there exists a region (from $y_\eta = 3$ up to 10–20) where $-E_\varepsilon$ becomes positive. This is consistent with the findings of different DNS using the FENE-P model for polymer solutions [13, 18, 19], that the correlation of u' and the streamwise polymer stress is positive close to the wall but changes its sign away from the wall. This implies that, in this region, a fraction of the elastic energy, which is accumulated at the outer region ($-E_\varepsilon < 0$ at $y_\eta > 20$), is transferred backward to the turbulent kinetic energy. Moreover, both E_d and $-E_\varepsilon$ are found to be highly dependent on We_τ and β. Their behaviors are not scaled by the microscale based on the effective viscosity nor by an outer scale such as δ.

To understand the relation between the energy-transfer rate $-E_\varepsilon$ further, we have examined instantaneous flow fields. Figure 16 shows the instantaneous field of $-E_\varepsilon$ and the velocity vector in an arbitrarily chosen cross-section of the (y, z) plane. Note that the axes are non-dimensionalized by the effective viscosity. In Fig. 16(a) (fluid C as an example of low-$DR\%$ flow), we can observe a number of eddies near the walls, especially in the buffer layer, which has been widely accepted for the Newtonian fluids. The

meaningful variation of $-E_\varepsilon$ is also limited only in the buffer layer. Hence it can be said that large-scale eddies, which occur in the outer layer, are not related with the viscoelastic contribution of flow at low $DR\%$. For fluid E1 with high $DR\%$, near-wall vortical structures are suppressed and only rather large-scale eddies can be found: see Fig. 16(b). Moreover, regions of $-E_\varepsilon > 0$ are observed not only at the near-wall region but also at the outer region, and coincide well with the positions of a quasi-streamwise vortex, indicating some relationship between the viscoelastic contribution and the local flow topology. Similar results are observed for other high-$DR\%$ cases.

3.7.2. Relation to flow topology

Topological analysis through the so-called (R, Q) invariant map is useful for describing flow fields with large data sets generated by DNS [53, 54, 55, 56]. Chong *et al.* [53] carried out a classification of the various types of three-dimensional flow patterns, based on the structure in the space of invariants of the velocity gradient tensor

$$a_{ij} = \frac{\partial u_i}{\partial x_j}. \tag{27}$$

The second and third invariants of the characteristic equation for the eigenvalues of a_{ij} are given by

$$Q = \frac{1}{2}\left(\text{trace}[a_{ij}]^2 - \text{trace}\left[a_{ij}^2\right]\right), \tag{28}$$

$$R = -\det\left[a_{ij}\right]. \tag{29}$$

Note here that the first invariant is equivalent to Eq. (1). A solution to the characteristic equation at each point determines a local linearized flow pattern. The discriminant

$$D = 27R^2 + 4Q^3 = 0 \tag{30}$$

defines the transition between rotational and extensional flows: for $D < 0$, the flow is extensional. Four local-flow topologies, which can occur in an incompressible flow, are determined by the (R, Q) map, as given in Fig. 17. The four classifications are unstable focus/contracting (UF), stable focus/stretching (SF), stable node/saddle/saddle (SN), and unstable node/node/saddle (UN), respectively (reading from the top-right corner counter-clockwise in the figure). In concrete terms, in the upper right-hand (first quadrant) region the

local flow has uniaxial compression along one axis with outward spiraling along the plane in the other directions; in the upper left-hand region it behaves in the opposite manner. It should be emphasized that both SF and UF correspond to rotational flow, i.e., vortex. In the lower region of the map, SN represents uniaxial elongation and biaxial compression, and UN is the reverse behavior (biaxial elongation and uniaxial compression). The typical teardrop shape (see, for instance, [56, 57]) for the present flows remains practically unchanged (figure not shown): in the buffer region the local-flow pattern is most likely to lie in SF and UN.

Table 3 shows percentages of occurrence of each flow pattern at $y_\eta = 5$, 30 and 94 for three kinds of fluids: i.e., fluid C (as a low-$DR\%$ case), E1 (as a high-$DR\%$ case), and E2 (as a high-$DR\%$ at different $Re_{\tau 0}$). In order to examine the influence of viscoelastic fluid on the topology of the turbulent flow field, we showed the results for each of $-E_\varepsilon > 0$ and $-E_\varepsilon < 0$. Here the absolute values of (R, Q) are not considered. In all cases of the fluids, a correlation between $-E_\varepsilon$ and the local-flow pattern is observed: if $-E_\varepsilon > 0$, SF is dominant; if $-E_\varepsilon < 0$, UF is dominant, implying that the vortex stretching and compressing are related to the gain and loss from the elastic energy (to the turbulent kinetic energy), respectively. Such a tendency is prominent at $y_\eta = 5$ in the buffer layer (or viscous sublayer) and also at $y_\eta = 30$ in the elastic layer, which exists for high-$DR\%$ cases such as fluids E1 and E2. This is consistent with the finding that a localized energy-gain region exists in the buffer and elastic layers, as shown in Fig. 15, and that turbulent vortical motions are dominant in this region, as in Fig. 16(b). In the case of low $DR\%$ (or at low We_τ), it is clearly seen that, away from the wall, the preferences for SF (with $-E_\varepsilon > 0$) and UF (with $-E_\varepsilon < 0$) are significantly reduced. Recalling that the SF and UF, respectively, represent strong rotational flow and unsteady vortex, this result is an indication that a drag-reduced flow involves energy transformation between kinetic energy and elastic energy through the induction and damping of eddies and that the elastic layer (in which the energy transformation is active) expands to the outer layer in a high $DR\%$ case.

4. Conclusion

We have studied the turbulent channel flow of viscoelastic fluid using DNS with the Giesekus constitutive equation at two different Reynolds numbers of $Re_{\tau 0} = 150$ and 395. Two simulations for Newtonian flow and eight

simulations for surfactant solutions were performed to systematically investigate drag-reduced turbulent flows with varying values of two parameters: the Weissenberg number (We_τ) and the viscosity ratio (β) of the solvent viscosity to the total zero-shear rate solution viscosity. We present various turbulence statistics and analyzed their dependence on the parameters as well as the obtained drag-reduction rate. Energy transfer between the flow (kinetic energy) and additives (elastic energy) was examined through transport equations and flow topology, from which the mechanism for drag reduction was elucidated.

It was shown that high drag reduction can be achieved by suppressing the turbulent contribution for a high Weissenberg-number fluid, and/or by decreasing the viscosity ratio (accompanied by a decrease of the effective viscosity). An offset in the logarithmic region of the mean-velocity profile increased as a function of We_τ, but not of β. A highly drag-reduced turbulent flow at a high Reynolds-number was caused mainly by the viscoelastic effect in the elastic layer whereas the outer-layer flow remains almost Newtonian flow and hardly affects the drag reduction, implying the existence of a shear-induced structure that was observed for experiments of surfactant solutions.

The budget balance of the turbulence intensity was discussed focusing on the viscoelastic contribution term, especially the energy-transfer rate (between turbulent kinetic energy to elastic energy), which is absent in Newtonian-fluid flow. We found that the viscoelastic contribution term for highly drag-reduced turbulent flow worked as a gain of turbulent energy at around $y_\eta \approx 8$ (in wall units), whereas it acted as a loss in almost the entire channel. Moreover, the energy-transfer rate $-E_\varepsilon$ was also studied focusing on its relation to turbulent flow topologies related to the invariants of the velocity gradient tensor. In the near-wall region including the elastic layer of a highly drag-reduced flow, a positive area of $-E_\varepsilon$ is closely associated with vortex stretching that produces turbulent kinetic energy from stored elastic energy, whereas a negative one causes vortex compression (energy loss).

Acknowledgements

The present computations were performed using supercomputing resources at the Cyberscience Center at Tohoku University. This work was conducted in the Research Center for Holistic Computational Science (Holcs). The third author (B.Y.) expresses appreciation for the support of the National Science Foundation of China (No. 50876114, No. 50506017 and No. 10602043), SRF

for ROCS, SEM Specialised Research Fund for the Doctoral Programme of Higher Education of China (No. 20050425006) and the Key Project of the Chinese Ministry of Education (No. 106034).

References

[1] B.A. Toms, *Some observations on the flow of linear polymer solutions through straight tubes at large Reynolds numbers*, Proc. First Int. Congress on Rheology (1948), pp. 135–141.

[2] J.L. Lumley, *Drag reduction by additives*, Ann. Rev. Fluid Mech., 1 (1969), pp. 367–384.

[3] R.H. Nadolink and W.W. Haigh, *Bibliography on skin friction reduction with polymers and other boundary-layer additives*, ASME Appl. Mech. Rev., 48 (1995), pp. 351–460.

[4] A. Gyr and H.-W. Bewersdorff, *Drag reduction of turbulent flows by additives*, Kluwer Academic Pub., Dordrecht, 1995.

[5] C.M. White and M.G. Mungal, *Mechanics and prediction of turbulent drag reduction with polymer additives*, Ann. Rev. Fluid Mech., 40 (2008), pp. 235–256.

[6] F.-C. Li, Y. Kawaguchi, T. Segawa, and K. Hishida, *Reynolds-number dependence of turbulence structures in a drag-reducing surfactant solution channel flow investigated by particle image velocimetry*, Phys. Fluids, 17 (2005), 075104, 13 pp.

[7] F.-C. Li, Y. Kawaguchi, B. Yu, J.-J. Wei, and K. Hishida, *Experimental study of drag-reduction mechanism for a dilute surfactant solution flow*, Int. J. Heat Mass Transfer, 51 (2008), pp. 835–843.

[8] W.-H. Cai, F.-C. Li, H.-N. Zhang, X.-B. Li, B. Yu, J.-J. Wei, Y. Kawaguchi, and K. Hishida, *Study on the characteristics of turbulent drag-reducing channel flow by particle image velocimetry combining with proper orthogonal decomposition analysis*, Phys. Fluids, 21 (2009), 115103, 12 pp.

[9] R. Sureshkumar, A.N. Beris, and R.A. Handler, *Direct numerical simulation of the turbulent channel flow of a polymer solution*, Phys. Fluids, 9 (1997), pp. 743–755.

[10] J.M.J. Den Toonder, M.A. Hulsen, G.D.C. Kuiken, and F.T.M. Nieuwstadt, *Drag reduction by polymer additives in a turbulent pipe flow: numerical and laboratory experiments*, J. Fluid Mech., 337 (1997), pp. 193–231.

[11] C.D. Dimitropoulos, R. Sureshkumar, and A.N. Beris, *Direct numerical simulation of viscoelastic turbulent channel flow exhibiting drag reduction: effect of the variation of rheological parameters*, J. Non-Newtonian Fluid Mech., 79 (1998), pp. 433–468.

[12] S. Sibilla and A. Baron, *Polymer stress statistics in the near-wall turbulent flow of a drag-reducing solution*, Phys. Fluids, 14 (2002), pp. 1123–1136.

[13] E. de Angelis, C.M. Casciola, and R. Piva, *DNS of wall turbulence: Dilute polymers and self-sustaining mechanisms*, Comput. Fluids, 31 (2002), pp. 495–507.

[14] T. Min, J.Y. Yoo, H. Choi, and D.D. Joseph, *Drag reduction by polymer additives in a turbulent channel flow*, J. Fluid Mech., 486 (2003), pp. 213–223.

[15] K.D. Housiadas and A.N. Beris, *An efficient fully implicit spectral scheme for DNS of turbulent viscoelastic channel flow*, J. Non-Newtonian Fluid Mech., 122 (2004), pp. 243–262.

[16] K.D. Housiadas and A.N. Beris, *Characteristic scales and drag reduction evaluation in turbulent channel flow of nonconstant viscosity viscoelastic fluids*, Phys. Fluids, 16 (2004), pp. 1581–1586.

[17] C.D. Dimitropoulos, Y. Dubief, E.S.G. Shaqfeh, and P. Moin, *Direct numerical simulation of polymer-induced drag reduction in turbulent boundary layer flow of inhomogeneous polymer solutions*, J. Fluid Mech., 556 (2006), pp. 153–162.

[18] C.-F. Li, R. Sureshkumar, and B. Khomami, *Influence of rheological parameters on polymer induced turbulent drag reduction*, J. Non-Newtonian Fluid Mech. 140 (2006), pp. 23–40.

[19] K. Kim, C.-F. Li, R. Sureshkumar, S. Balachandar, and R.J. Adrian, *Effects of polymer stresses on eddy structures in drag-reduced turbulent channel flow*, J. Fluid Mech., 584 (2007), pp. 281–299.

[20] H. Giesekus, *A simple constitutive equation for polymer fluids based on the concept of deformation dependent tensorial mobility*, J. Non-Newtonian Fluid Mech., 11 (1982), pp. 69–109.

[21] J. Wei, Y. Kawaguchi, B. Yu, and Z. Feng, *Rheological characteristics and turbulent friction drag and heat transfer reductions of a very dilute cationic surfactant solution*, Trans. ASME C: J. Heat Transfer, 128 (2006), pp. 977–983.

[22] H. Suzuki, K. Ishihara, and H. Usui, *Numerical study on a drag-reducing flow with surfactant additives*, In: Proceedings 3rd Pacific Rim Conference on Rheology (2001).

[23] B. Yu and Y. Kawaguchi, *Direct numerical simulation of viscoelastic drag-reducing flow: a faithful finite difference method*, J. Non-Newtonian Fluid Mech., 116 (2004), pp. 431–466.

[24] B. Yu, F. Li, and Y. Kawaguchi, *Numerical and experimental investigation of turbulent characteristics in a drag-reducing flow with surfactant additives*, Int. J. Heat and Fluid Flow, 25 (2004), pp. 961–974.

[25] B. Yu and Y. Kawaguchi, *Parametric study of surfactant-induced drag-reduction by DNS*, Int. J. Heat and Fluid Flow, 27 (2006), pp. 887–894.

[26] Y. Kagawa, B. Yu, Y. Kawaguchi, H. Kawamura, and Y. Shiraishi, *Turbulent heat transfer of viscoelastic fluid flow accompanied by drag reduction with DNS analysis*, Prog. Comput. Fluid Dyn., 8 (2008), pp. 477–485.

[27] J. Zhu and W. Rodi, *A low dispersion and bounded convection scheme*, Comput. Methods Appl. Mech. Engng., 92 (1991), pp. 87–96.

[28] S.K. Choi, H.Y. Nam, and M. Cho, *A comparison of higher-order bounded convection schemes*, Comput. Methods Appl. Mech. Engng., 121 (1995), pp. 281–301.

[29] R.D. Dean, *Reynolds number dependence of skin friction and other bulk flow variables in two-dimensional rectangular duct flow*, Trans. ASME I: J. Fluids Eng., 100 (1978), pp. 215–223.

[30] P.S. Virk, *Drag reduction in rough pipes*, J. Fluid Mech., 45 (1971), pp. 225–246.

[31] P.S. Virk, *An elastic sublayer model for drag reduction by dilute solutions of linear macromolecules*, J. Fluid Mech., 45 (1971), pp. 417–440.

[32] M.D. Warholic, H. Massah, and T.J. Hanratty, *Influence of drag-reducing polymers on a turbulence: effects of Reynolds number, concentration and mixing*, Exps. Fluids, 27 (1999), pp. 461–472.

[33] M.D. Warholic, G.M. Schmidt, and T.J. Hanratty, *The influence of a drag-reducing surfactant on a turbulent velocity field*, J. Fluid Mech., 388 (1999), pp. 1–20.

[34] P.K. Ptasinski, B.J. Boersma, F.T.M. Nieuwstadt, M.A. Hulsen, B.H.A.A. Van den Brule, and J.C.R. Hunt, *Turbulent channel flow near maximum drag reduction: simulations, experiments and mechanisms*, J. Fluid Mech., 490 (2003), pp. 251–291.

[35] J.L. Zakin, J. Myska, and Z. Chara, *New limiting drag reduction and velocity profile asymptotes for nonpolymeric additives systems*, AIChE J., 42 (1996), pp. 3544–3546.

[36] H. Usui, T. Itoh, and T. Saeki, *On pipe diameter effects in surfactant drag-reducing pipe flows*, Rheol. Acta., 37 (1998), pp. 122–128.

[37] K. Gasljevic, G. Aguilar, and E.F. Matthys, *An improved diameter scaling correlation for turbulent flow of drag-reducing polymer solutions*, J. Non-Newtonian Fluid Mech., 984 (1999), pp. 131–148.

[38] K. Fukagata, K. Iwamoto, and N. Kasagi, *Contribution of Reynolds stress distribution to the skin friction in wall-bounded flows*, Phys. Fluids, 14 (2002), pp. L43–L76.

[39] Y.-X. Hou V.S. R. Somandepalli, and M.G. Mungal, *A technique to determine total shear stress and polymer stress profiles in drag reduced boundary layer flows*, Exp. Fluids, 40 (2006), pp. 589–600.

[40] R.A. Antonia, M. Teitel, J. Kim, and L.W.B. Browne, *Low-Reynolds-number effects in a fully developed turbulent channel flow*, J. Fluid Mech., 236 (1992), pp. 579–605.

[41] H. Abe, H. Kawamura, and Y. Matsuo, *Direct numerical simulation of a fully developed turbulent channel flow with respect to the Reynolds number dependence*, Trans. ASME I: J. Fluids Eng., 123 (2001), pp. 382–393.

[42] J. Kim, P. Moin, and R. Moser, *Turbulence statistics in fully developed channel flow at low Reynolds number*, J. Fluid Mech., 177 (1987), pp. 133–166.

[43] G. Comte-Bellot, *Contribution a l'étude de la turbulence de conduite*, Doctoral thesis, University of Grenoble, 1963.

[44] J.L. Lumley and G.R. Newman, *The return to isotropy of homogeneous turbulence*, J. Fluid Mech., 82 (1977), pp. 161–178.

[45] J. Piquet, *Turbulent Flows: Models and Physics*, Springer-Verlag, Berlin, 1999.

[46] J. Jovanović, M. Pashtrapanska, B. Frohnapfel, F. Durst, J. Koskinen, and K. Koskinen, *On the mechanism responsible for turbulent drag reduction by dilute addition of high polymers: theory, experiments, simulations, and predictions*, Trans. ASME I: J. Fluids Eng., 126 (2006), pp. 118–130.

[47] B. Frohnapfel, P. Lammers, J. Jovanović, and F. Durst, *Interpretation of the mechanism associated with turbulent drag reduction in terms of anisotropy invariants*, J. Fluid Mech., 577 (2007), pp. 457–466.

[48] T. Watanabe, A. Saito, M. Motozawa, and Y. Kawaguchi, *Spatial Structure in the Drag Reducing Channel Flow of Viscoelastic Fluid*, In: Proceedings the 6th Symposium on Turbulence, Heat and Mass Transfer (2009).

[49] I.A. Kadoma, C. Ylitalo, and J.W. van Egmond *Structural transitions in wormlike micelles*, Rheol. Acta, 36 (1997), pp. 1–12.

[50] M. Itoh, S. Tamano, K. Yokota, and M. Ninagawa, *Velocity measurement in turbulent boundary layer of drag-reducing surfactant solution*, Phys. Fluids, 17 (2005), 075107, 9 pp.

[51] S. Tamano, M. Itoh, T. Inoue, K. Kato, and K. Yokota *Turbulence statistics and structures of drag-reducing turbulent boundary layer in homogeneous aqueous surfactant solutions*, Phys. Fluids, 21 (2009), 045101, 19 pp.

[52] H. Massah and T.J. Hanratty, *Added stresses because of the presence of FENE-P bead-spring chains in a random velocity field*, J. Fluid Mech., 337 (1997), pp. 67–101.

[53] M.S. Chong, A.E. Perry, and B.J. Cantwell, *A general classification of three-dimensional flow fields*, Phys. Fluids, 2 (1990), pp. 765–777.

[54] A.E. Perry and M.S. Chong, *Topology of flow patterns in vortex motions and turbulence*, Appl. Sci. Res., 53 (1994), pp. 357–374.

[55] J. Soria and B. J. Cantwell, *Topological visualisation of focal structure in free shear flow*, Appl. Sci. Res., 53 (1994), pp. 375–386.

[56] J. Soria, R. Sondergaard, B.J. Cantwell, M.S. Chong, and A.E. Perry, *A study of the fine-scale motions of incompressible time-developing mixing layers*, Phys. Fluids, 6 (1994), pp. 871–884.

[57] W. Li, P.A. Stone, and M.D. Graham *Viscoelastic nonlinear traveling waves and drag reduction in plane Poiseuille flow* in *IUTAM Symp. on Laminar Turbulent Transition and Finite Amplitude Solutions*, Fluid Mech. and its Appl., 77, T. Mullin and R.R. Kerswell, eds., Springer, Netherlands, 2005, pp. 173–193.

Table 1: Reynolds number and computational domain size: L_i, N_i and Δi are box length, grid number and spatial resolution in the i-direction, respectively.

Fluid	A1	A2	B, C, D1, E1, F	D2, E2
$L_x^* \times L_y^* \times L_z^*$	$10.0 \times 2.0 \times 5.0$	$6.4 \times 2.0 \times 3.2$	$12.8 \times 2.0 \times 6.4$	$12.8 \times 2.0 \times 6.4$
$N_x \times N_y \times N_z$	$128 \times 128 \times 128$	$256 \times 256 \times 256$	$128 \times 128 \times 128$	$256 \times 256 \times 256$
Δx^*	0.08	0.025	0.10	0.050
Δz^*	0.05	0.0125	0.05	0.025
$\Delta y^*_{\min}$	0.00149	0.00095	0.00149	0.00075
$\Delta y^*_{\max}$	0.03013	0.01393	0.03013	0.01506

Table 2: Computational parameters ($Re_{\tau 0}, We_\tau, \beta$) and important results of mean flow variables ($U_{\rm m}^+, \eta_{\mathit{eff}}, Re_{\rm m}, Re_\tau, DR\%$). The cases are arranged in ascending order of $DR\%$ (except for the order between fluids E1 and E2).

Fluid	$Re_{\tau 0}$	We_τ	β	$U_{\rm m}^+$	$\eta_{\mathit{eff}}/\eta_0$	$Re_{\rm m}$	Re_τ	$DR\%$
A1	150	0	1.0	15.2	1.000	4570	150	—
A2	395	0	1.0	18.0	1.000	14200	395	—
B	150	10	0.8	16.3	0.962	5100	156	10.4
C	150	10	0.5	17.1	0.885	5780	169	14.7
D1	150	11	0.5	17.8	0.870	6130	173	20.0
D2	395	11	0.5	21.0	0.870	19000	454	20.0
E1	150	30	0.5	25.9	0.690	11300	217	52.2
E2	395	30	0.5	29.6	0.690	33900	571	52.5
F	150	30	0.3	29.6	0.518	17100	290	61.0
G	150	40	0.5	30.1	0.654	13800	229	64.6

Table 3: Relation between $-E_\varepsilon$, and local-flow pattern defined by topological classification at several wall-normal positions. The values are indicated in percentage, and boldface represents the most dominant flow pattern at each height.

		$y_\eta = 5$		$y_\eta = 30$		$y_\eta = 94$	
		$-E_\varepsilon > 0$	$-E_\varepsilon < 0$	$-E_\varepsilon > 0$	$-E_\varepsilon < 0$	$-E_\varepsilon > 0$	$-E_\varepsilon < 0$
	SF (%)	**51**	34	**34**	**37**	**37**	**38**
Fluid	UF (%)	24	**38**	31	34	30	34
D1	UN (%)	16	16	25	22	23	19
	SN (%)	8	10	10	7	10	9
	SF (%)	**42**	35	**46**	31	**44**	**36**
Fluid	UF (%)	30	**37**	34	**42**	37	34
E1	UN (%)	15	16	13	20	13	23
	SN (%)	13	12	7	7	6	7
	SF (%)	**40**	35	**41**	33	**40**	**36**
Fluid	UF (%)	32	**36**	35	**42**	32	34
E2	UN (%)	15	17	17	18	20	23
	SN (%)	13	12	7	7	8	8

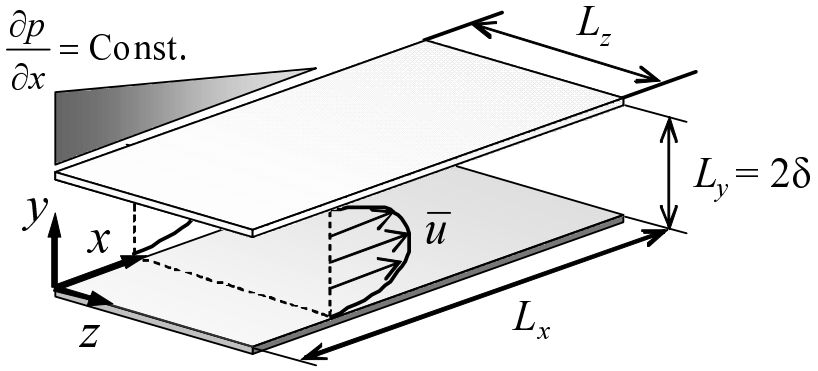

Figure 1: Schematic of the flow geometry.

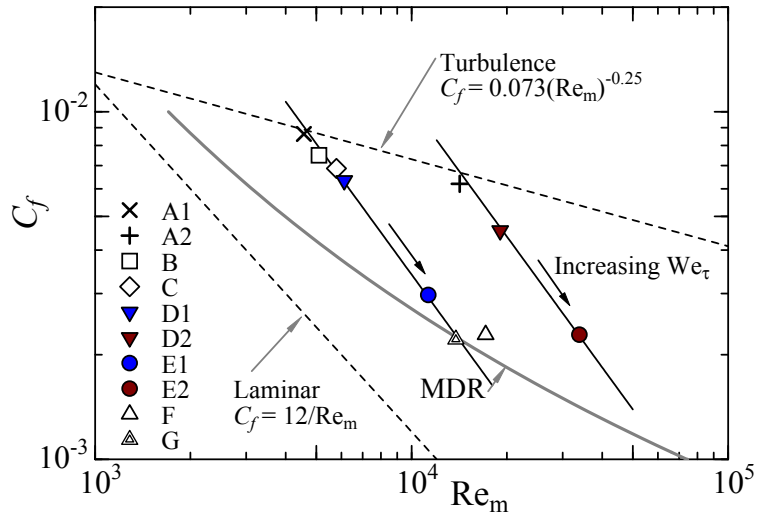

(a)

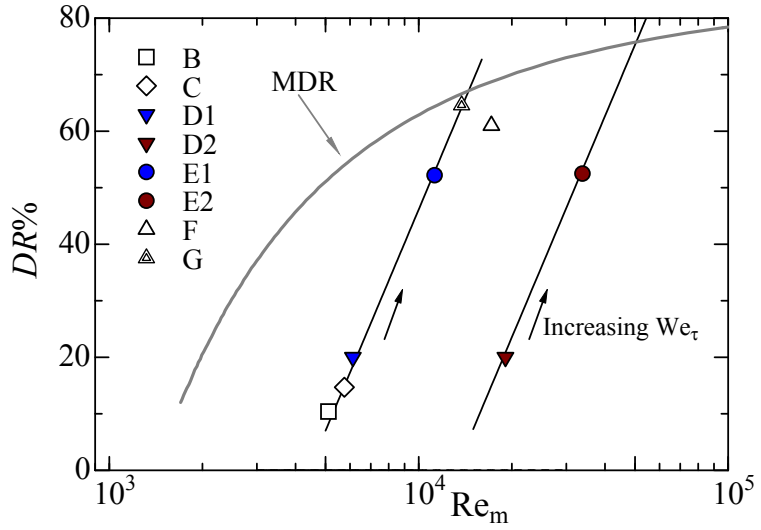

(b)

Figure 2: (a) Friction coefficient as a function of solvent bulk Reynolds number. (b) $DR\%$ *versus* Re_{m}. The maximum drag-reduction asymptote (MDR) proposed by Virk [30] is plotted for reference. For indexes (and the parameters) of fluids, see Table 2.

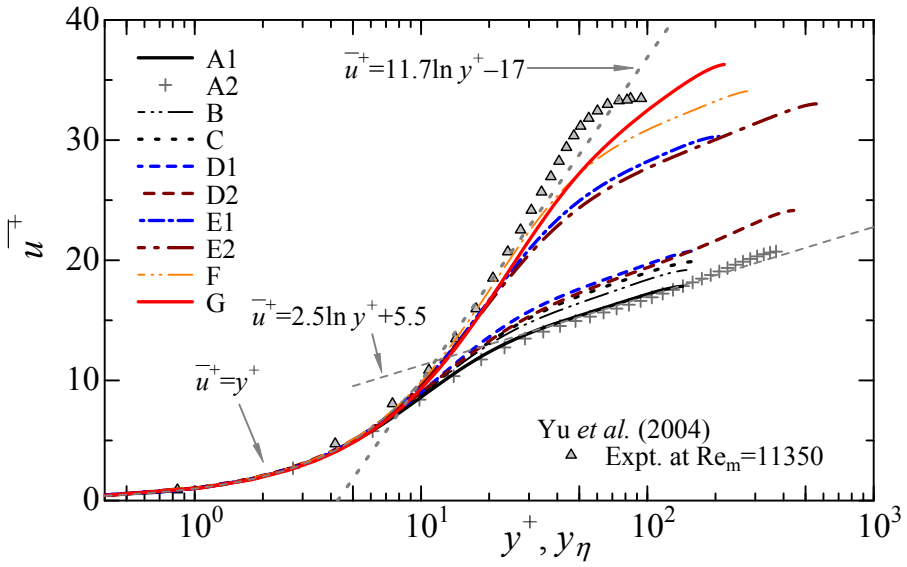

Figure 3: Mean velocity profile in comparison with data from the PIV experiment [24]. Also shown are the theoretical wall laws in the viscous sublayer and the logarithmic layer for Newtonian flow, and the empirical law (so-called Virk's ultimate profile) for drag-reduced flow [31].

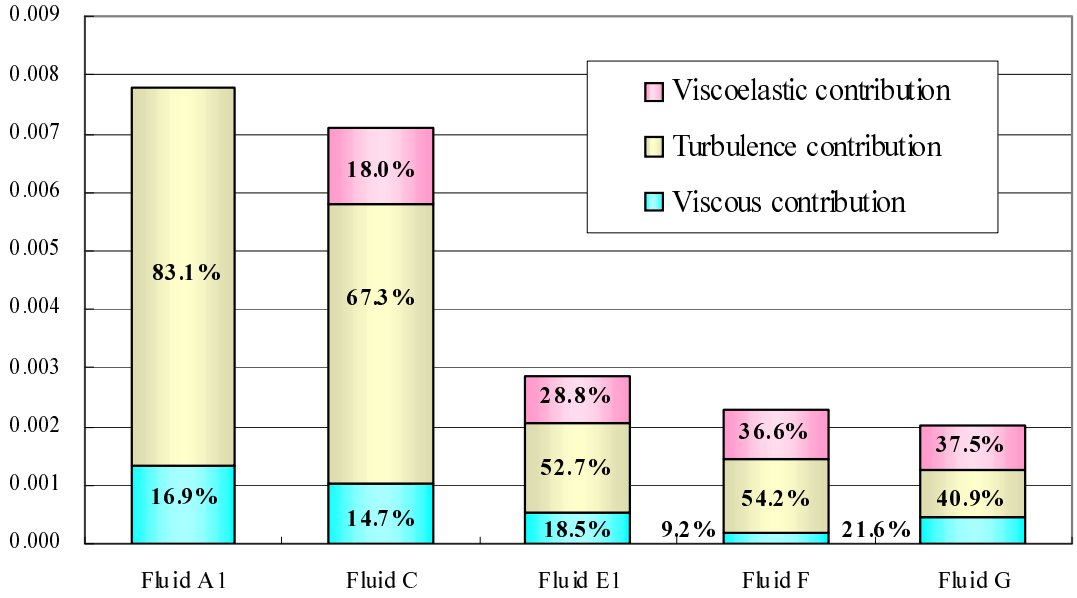

Figure 4: Fractional contribution to friction coefficient.

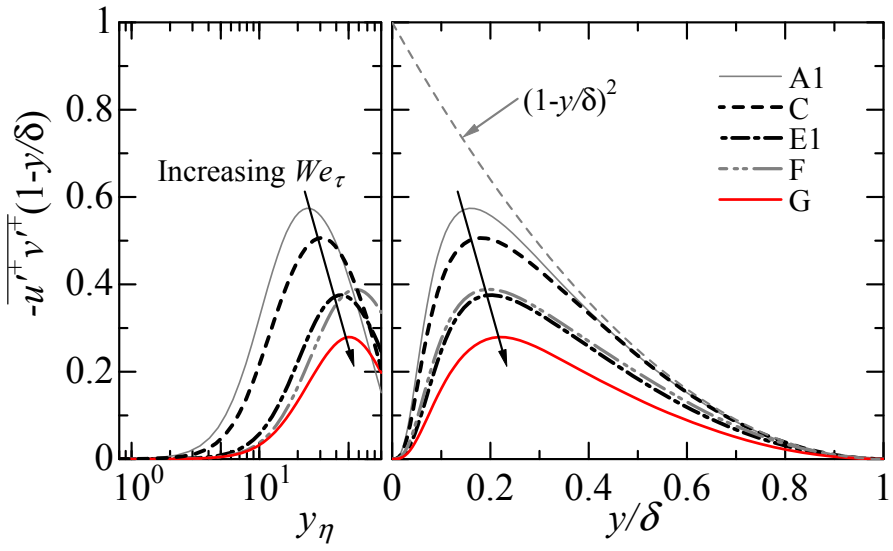

Figure 5: Distribution of Reynolds shear stress weighted by the linear function of y/δ.

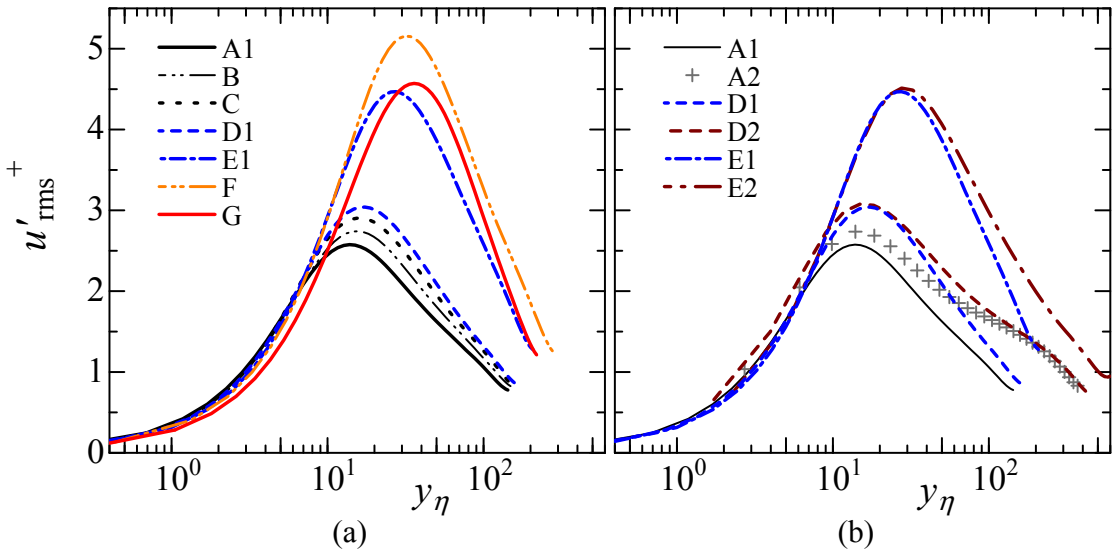

Figure 6: Root-mean-square of the streamwise velocity fluctuation, u'^{+}_{rms}: (a) different values of the rheological parameters at $Re_{\tau 0} = 150$; (b) comparison between $Re_{\tau 0} = 150$ and 395 at the same values of the rheological parameters.

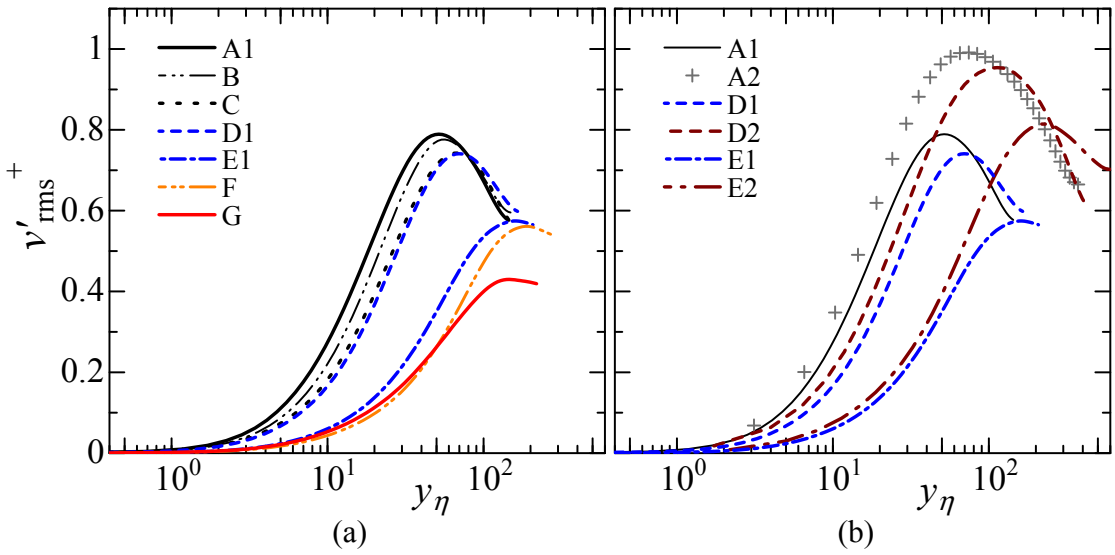

Figure 7: Same as Fig. 6, but for v'^{+}_{rms}.

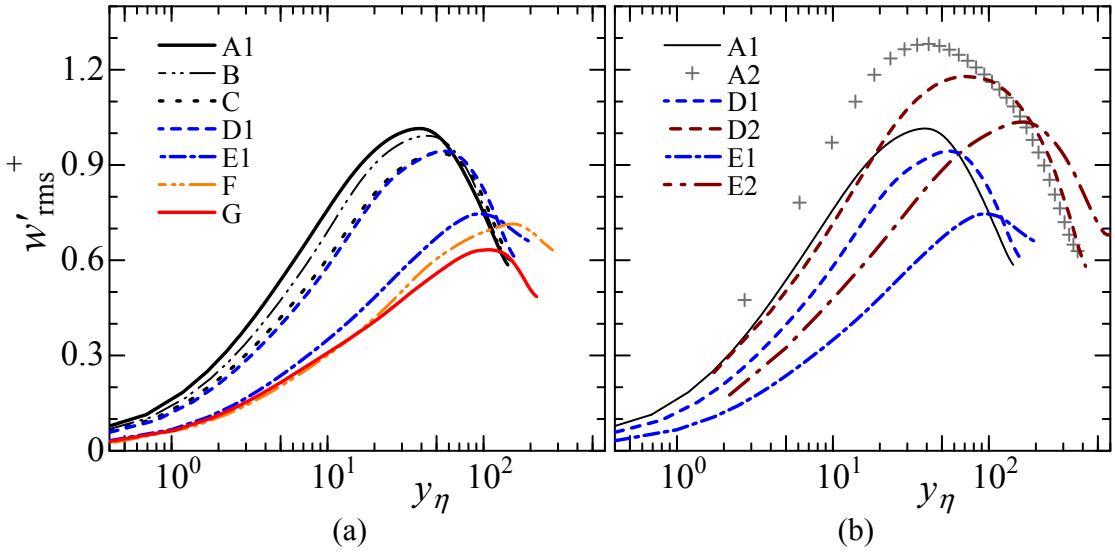

Figure 8: Same as Fig. 6, but for w'^{+}_{rms}.

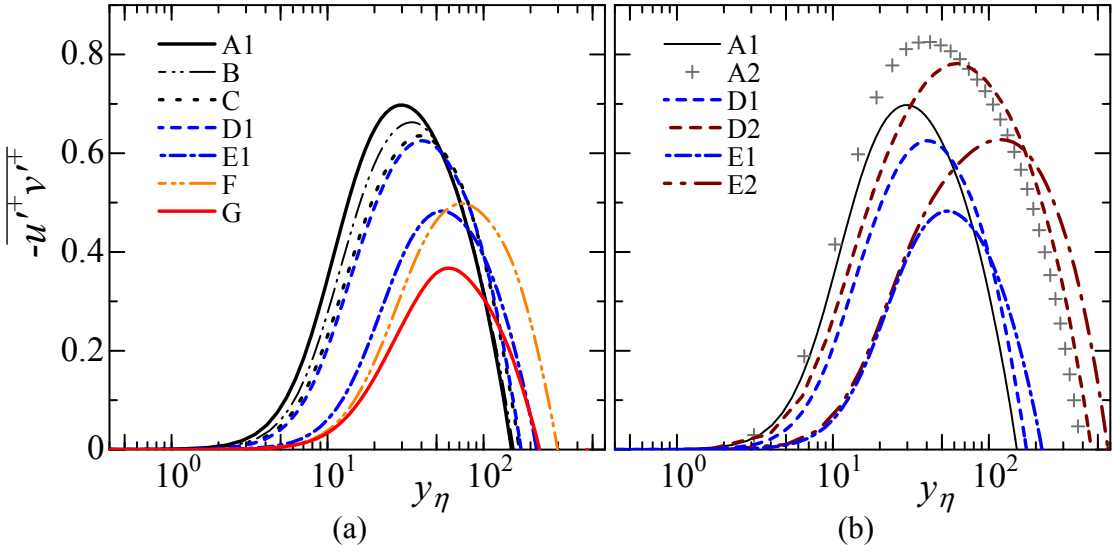

Figure 9: Same as Fig. 6, but for Reynolds shear stress $-\overline{u'^{+}v'^{+}}$.

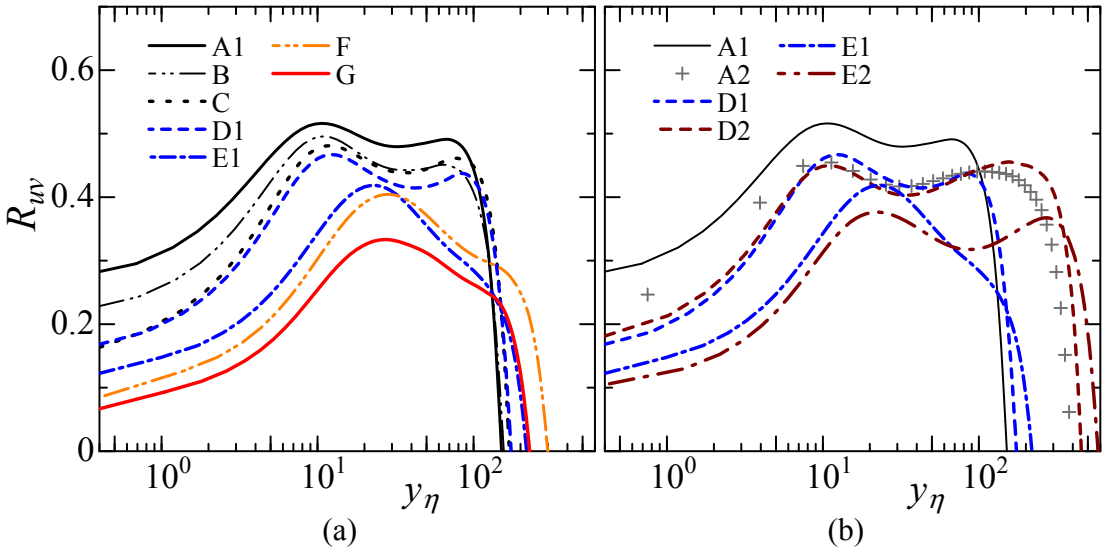

Figure 10: Same as Fig. 6, but for the cross-correlation coefficient of u' and v'.

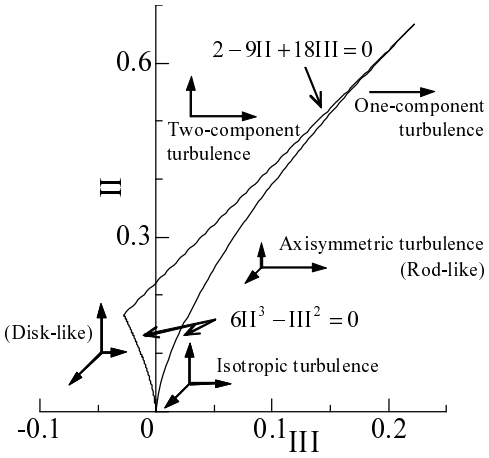

(a)

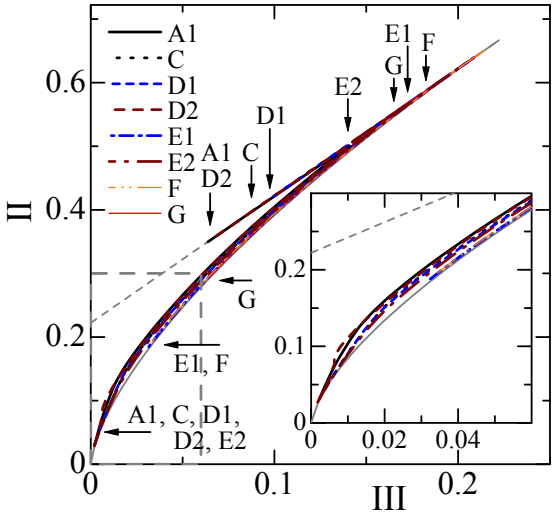

(b)

Figure 11: (a) Anisotropy-invariant map showing the limiting states of turbulence. Thick arrows represent the turbulent fluctuations that correspond to each of the limiting states. (b) Anisotropy-invariant mapping of drag-reducing turbulent channel flows, with an enlargement of trajectories of data around the channel core region. Vertical arrows indicate the value in the wall vicinity for each case, and horizontal arrows indicate the value at the channel center. The inset in (b) is an enlargement of the framed region.

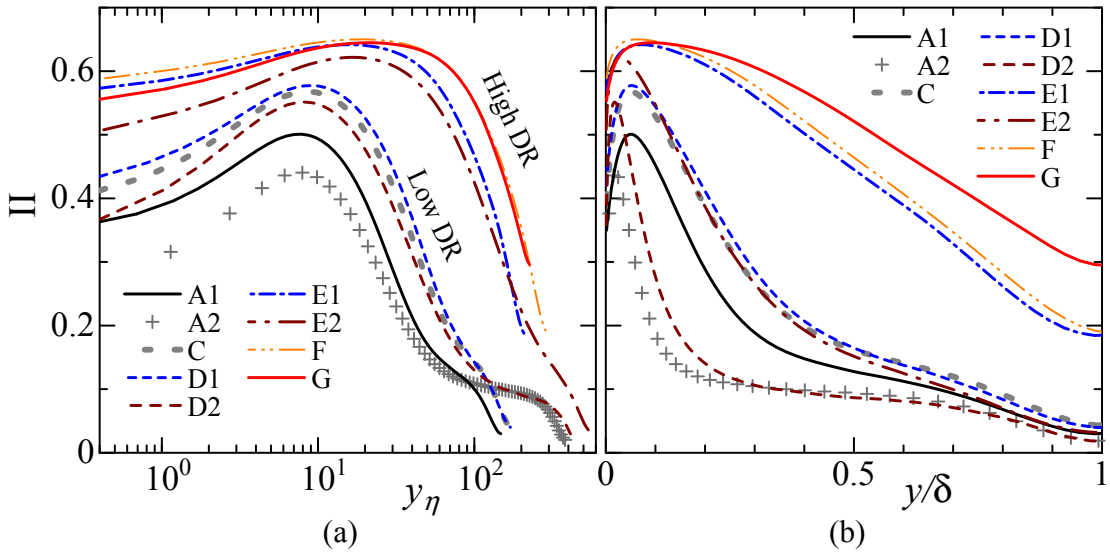

Figure 12: Replot of second invariant II of the Reynolds stress tensor against the wall-normal distance: (a) inner scaling, (b) outer scaling.

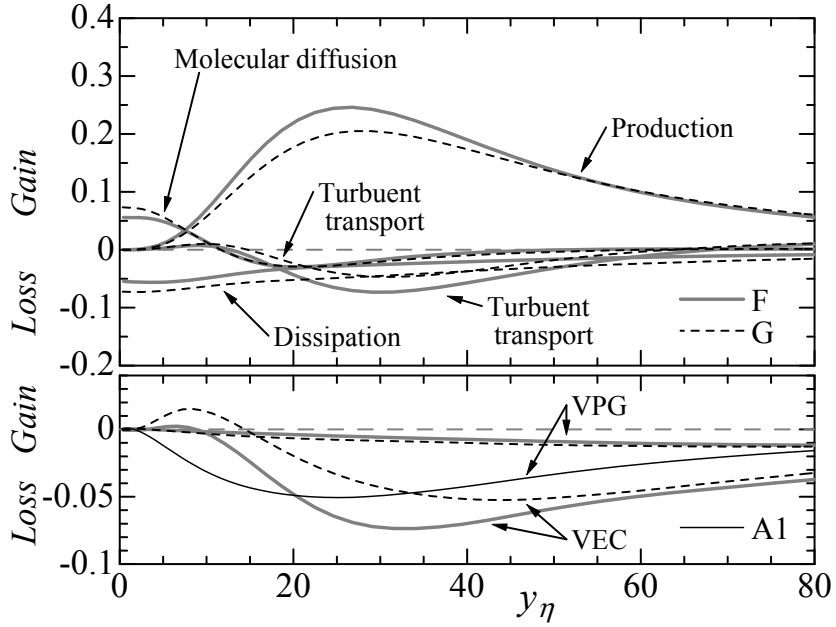

Figure 13: Budget of Reynolds stress $\overline{u'^+u'^+}$ for almost the same $DR\%$ cases. All terms are normalized by η_{eff}/u_τ^4. For fluid A1, only the VPG term is shown for comparison.

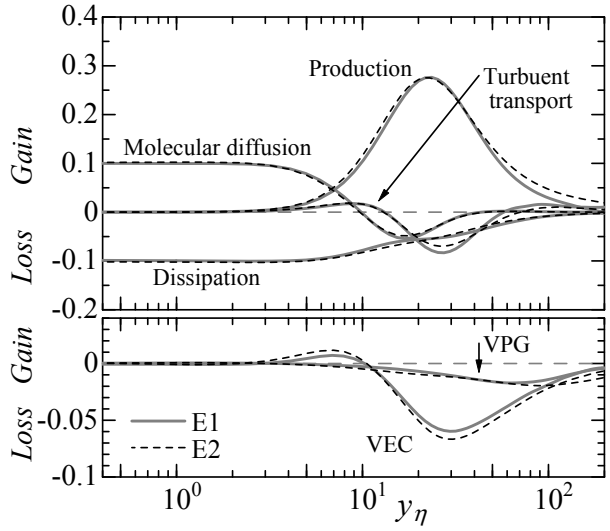

(a)

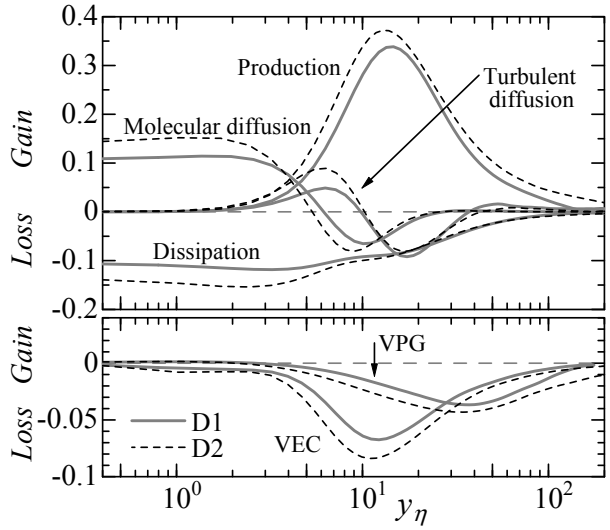

(b)

Figure 14: Reynolds-number dependence of budget of $\overline{u'^+u'^+}$ for flows with high $DR\%$ at $We_\tau = 30$ (a) and low $DR\%$ at $We_\tau = 11$ (b). All terms are normalized by η_{eff}/u_τ^4.

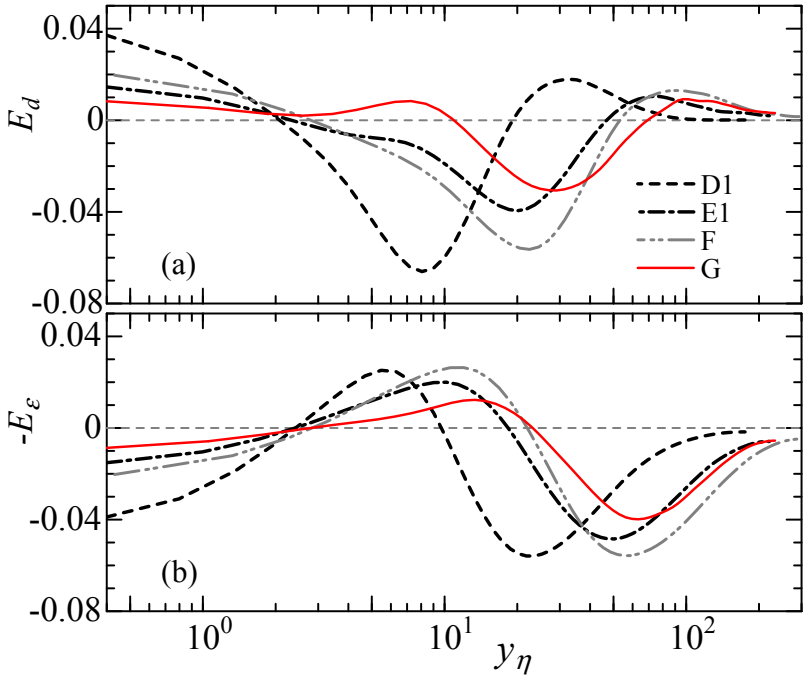

Figure 15: Distribution of viscoelastic contribution: E_d and E_ε.

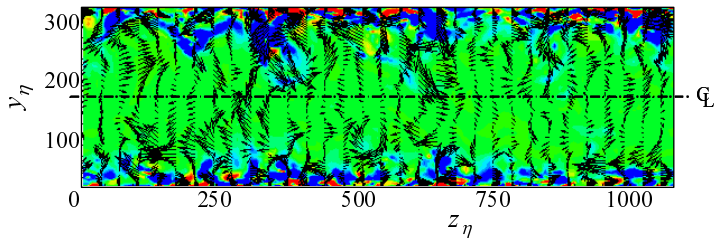

(a) Fluid C

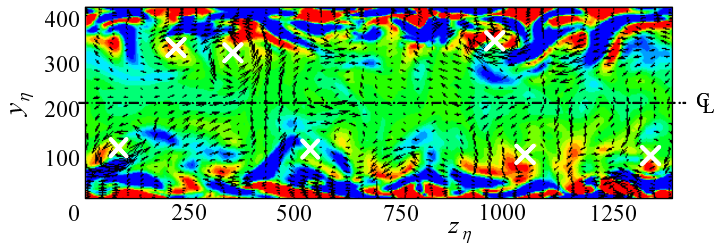

(b) Fluid E1

Figure 16: Instantaneous velocity vector and contour of $-E_\varepsilon$ in the (y, z)-plane: (a) Fluid C, (b) fluid E1. Vectors indicate (v', w'). A white marker of $\times$ in (b) represents the center of a quasi-streamwise vortex.

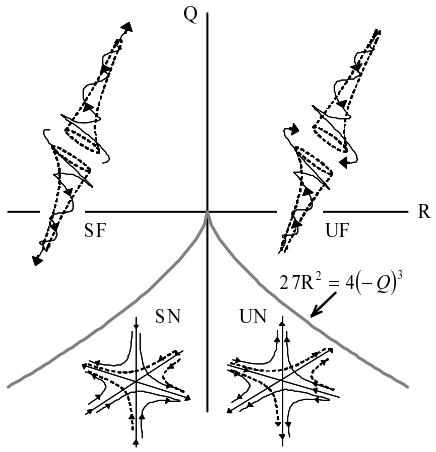

Figure 17: Topology classification of three-dimensional flow pattern, in the Q-R plane.